Abdelghafor, Zeiad; Taimuri, Ghalib; Kujala, Pentti; Wang, Youjiang; Hirdaris, Spyros

Numerical studies on tugboat performance during pushing operations

Published in:
Proceedings of the 12th International Workshop on Ship and Marine Hydrodynamics

DOI:
10.1088/1757-899X/1288/1/012003

Published: 09/08/2023

Document Version
Publisher's PDF, also known as Version of record

Please cite the original version:
Abdelghafor, Z., Taimuri, G., Kujala, P., Wang, Y., & Hirdaris, S. (2023). Numerical studies on tugboat performance during pushing operations. In S. Hirdaris, & D. Wan (Eds.), *Proceedings of the 12th International Workshop on Ship and Marine Hydrodynamics* Article 012003 (IOP Conference Series: Materials Science and Engineering; Vol. 1288). Institute of Physics Publishing. https://doi.org/10.1088/1757-899X/1288/1/012003

PAPER • **OPEN ACCESS**

Numerical studies on tugboat performance during pushing operations

IOP Conf. Series: Materials Science and Engineering 1288 (2023) 012003 doi:10.1088/1757-899X/1288/1/012003

Numerical studies on tugboat performance during pushing operations

Z Abdelghafor[1], G Taimuri[1,¥], P Kujala[1], Y Wang[2] and S Hirdaris[1]

1Aalto University, School of Engineering, Marine Technology Group, Espoo, Finland
2 Shanghai Jiao Tong University, School of Naval Architecture, Ocean & Civil Engineering, China
¥ Corresponding author: ghalib.taimuri@aalto.fi

Abstract. This paper introduces a RANS CFD methodology for the evaluation of tugboat dynamics during pushing operations. Two- and three- dimensional methods that respectively utilize "Dynamic Fluid Body Interactions - (DFBI)" and "Tug Force Equilibrium kinematics- (TFE)" are assessed and compared with the aim to better understand the influence of fluid modelling on ship dynamics. For the DFBI method, an unsteady RANS solver comprising of a dynamic fluid body interaction module and a contact mechanics coupling algorithm are used to predict the forces between a tugboat and an assisted ship. For the TFE method, a steady RANS method is applied and contact actions are calculated as a sum of the hydrodynamic forces on the hull and the propeller. Whereas DFBI accounts for the time variation of the contact forces, the TFE is more rapid and could be used to derive operational decision support criteria. To demonstrate the latter the TFE method is used to derive the pushing forces based on a set of 16 numerical simulations. It is concluded that irrespective of the model used the tugboat speed and orientation may amplify the pushing forces. This effect could be prominent, especially at slow speeds for which the sway force acts in opposite direction to the tug.

1. Introduction

Tugboats serve a range of berthing, salvage and ice-breaking shipping operations (see Figure 1) [1]. Yet, accidents that involve tugboat operations in confined waters and fairways are broadly associated with wrong decision making [2,3]. A review of accidents reported in the Baltic Sea area during the past two decades [4,5] reveals that poor communication during tug operations and the lack of pilotage assistance are the major causes of accidents between 1997 and 2011 [6]. To assess tug performance and safety during ship handling operations, it is essential to understand the influence of operational conditions on ship dynamics. This is particularly relevant for tug pulling and escorting operations for which the risk of accidents due to tug-ship hydrodynamic interactions should be minimized [7].

Tugboat maneuvering dynamics have been tackled using numerical and experimental methods with an eye on the hydrodynamic forces that act on the tugboat hull and appendages, the tug motions, and trajectories at different speeds [8]. Well validated RANS CFD methods could enable the broad derivation of improved hydrodynamic derivatives for use by modular maneuvering models [9]. An example of these models is the Mathematical Model Group (MMG) presented by Piaggio [10]. RANS CFD [11], potential flow (PF) hydrodynamics [12] or captive model tests [13,14] are distinct approaches that may be used to better understand ship - tug dynamics. Recently, [15,16] explored uncertainties of simulations as compared to experiments for the case where parallel and drifting tug operations interplay at lateral and longitudinal positions of a tanker.

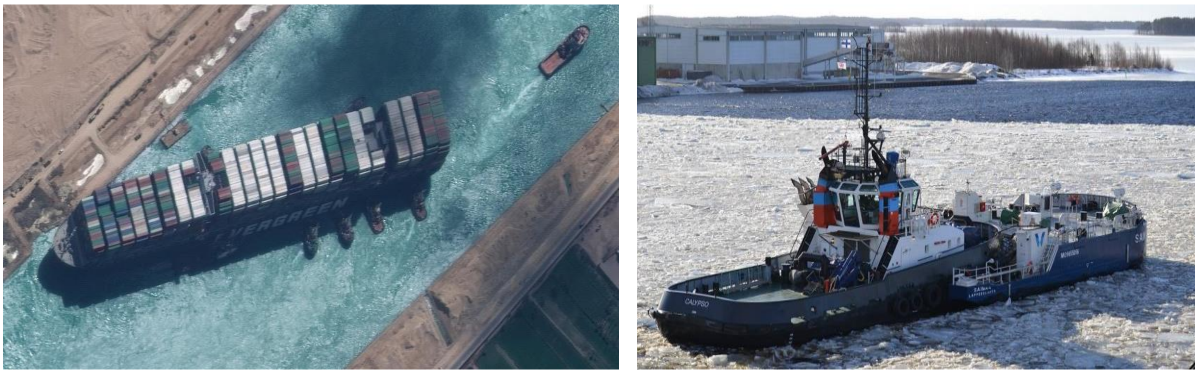

(a) (b)

Figure 1. Tugboats operations near ports and canals. (a) Tugboats assisting Ever Given [17]. (b) berths clearing from ice [18]

To date, most of the studies conducted to model the direct contact between a tugboat and an assisted vessel rely on the mathematical modular maneuvering models [19,20]. These models evaluate the hull, propeller, rudder, and other devices separately in addition to the external forces e.g., wind and waves. Ship-tug, propeller-hull, and propeller-rudder interactions are usually ignored. This paper pushes the state of the art by introducing the potential use of CFD methods for the evaluation of the contact forces applied on tugs during pushing mode assistance operations. Two- and three- dimensional methods that, respectively utilize "Dynamic Fluid Body Interactions - (DFBI)" and "Tug Force Equilibrium kinematics- (TFE)" are assessed and compared with the aim to understand the influence of fluid modelling on ship dynamics. Throughout the simulations, it is assumed that the behavior of the tugboat in oblique flow resembles the flow around a wet transom.

2. Theory

STARCCM+ was used for the numerical simulations [21]. The motions of the tugboat were simulated using the DFBI integrated into the equations of motion for all forces and moments. The aim of this process was to calculate accelerations in each time step.

2.1. *Equations of Fluid Flow and Turbulence models*

The flow was assumed turbulent, incompressible, and isothermal. The RANS method was adopted. The velocity and pressure were decomposed into mean ($\bar{u}$ and $\bar{p}$) and fluctuating (u' and p') parts. The mean flow velocities and pressures were obtained from the continuity and momentum equations

$$\frac{\partial \bar{u}_i}{\partial x_i} = 0 \tag{1}$$

$$\rho \frac{\partial \bar{u}_i}{\partial x_j} + \rho \frac{\partial}{\partial x_j}(\bar{u}_i \bar{u}_j) = -\frac{\partial \bar{p}}{\partial x_j} + \mu \frac{\partial^2 \bar{u}_i}{\partial x_j x_j} - \frac{\partial \tau_{ij}}{\partial x_j} + f_i \tag{2}$$

where $\rho\ [kg/m^3]$ is the density, $\mu\ [\ kg/m.s\ ]$ is the molecular viscosity, $u_i\ [m/s]$ is the velocity, $p\ [N/m^2]$ is the pressure, $\tau_{ij} = \rho\left(\overline{u_i' u_j'}\right)\ [N/m^2]$ is the Reynolds stress tensor, and $f_i\ [N]$ is the body force term. The appearance of the Reynolds stress term introduces nine additional unknowns to the equations for which additional equations must be obtained. In this study, the k-omega-SST turbulence model was used. This model is based on the combination of the k-ω and the k-ε models. The former model was activated in the near wall region. The latter was activated in the outer region of the boundary layer and the free shear layers. Implementation of the k-ω-SST turbulence introduced two additional equations for the turbulent kinetic energy $k\ [m^2/s^2]$ and the dissipation rate $\omega\ [m^2/s^3]$. The Reynolds stress term was replaced with the mean velocity gradients and Eddy viscosity $\mu_T\ [kg/m.s]$ as follows

$$\rho \frac{\partial k}{\partial t} + \rho \bar{u}_i \frac{\partial k}{\partial x_j} = \tau_{ij} \frac{\partial \bar{u}_i}{\partial x_j} - \beta^* \rho k \omega + \frac{\partial}{\partial x_j}[(\mu + \sigma^* \mu_T) \frac{\partial k}{\partial x_j}] \tag{3}$$

$$\rho\frac{\partial\omega}{\partial t}+\rho\bar{u}_i\frac{\partial\omega}{\partial x_j}=\frac{\gamma}{v_T}\tau_{ij}\frac{\partial\bar{u}_i}{\partial x_j}-\chi\rho\omega^2+\frac{\partial}{\partial x_j}\left[(\mu+\sigma_\omega\mu_T)\frac{\partial\omega}{\partial x_j}\right]+2\rho(1-F_1)\sigma_{\omega 2}\frac{1}{\omega}\frac{\partial k}{\partial x_j}\frac{\partial\omega}{\partial x_j} \tag{4}$$

In the above equations F_1 represents a blending function, which ensures that a k-ω formulation is used in the inner parts of the boundary layer and a k-ε behavior is achieved in the free-stream. The terms β^*, σ^*, γ, χ, σ_ω, $\sigma_{\omega 2}$ are model coefficients and may also depends on F_1.

In turbulent flows, the presence of viscosity affects the flow significantly near wall boundaries that may be sources of perturbations and vortices. The inner boundary layer region is further divided into three sublayers namely (a) viscous, (b) buffer, and (c) logarithmic. To capture the velocity gradient in the viscous sublayer a $y+\leq 1$ is needed. Thus, solving the flow through the viscous sub-layer is computationally expensive. This challenge is overcome by using wall functions, i.e., by setting a $y+$ value for the first cell next to the wall (i.e., in way of either the viscous or the logarithmic sublayers) to provide sufficiently accurate results. STAR-CCM+ utilizes the following blended wall function

$$u_*=\delta\sqrt{\frac{\mu|\vec{V}_{tangential}|}{\rho y}}+(1-\delta)C_\mu^{1/4}k^{1/2} \tag{5}$$

where u_* is the frictional velocity, δ is the blending function, $\vec{V}_{tangential}$ is the wall-tangential velocity vector, y is the wall distance, and C_μ is the turbulence model coefficient. In this study $30<y+<300\sim500$ and $y+<1$ were set in way of the log-layer and the viscous sublayer, respectively [22].

2.2. Computations of Motions and Contact Forces

Unless constraints to the body motions are defined, STAR-CCM+ solves the translation and rotation of the center of mass of the body at the earth-fixed coordinate system in all degrees of freedom. The equation of motion for translation and rotation in the earth-fixed coordinate system is defined as

$$m\frac{d\vec{V}_b}{dt}=\vec{F} \text{ and } M\frac{d\vec{\varpi}}{dt}+\vec{\varpi}\times M\vec{\varpi}=\vec{H} \tag{6}$$

where $\vec{V}_b$ $[m/s]$ is the velocity vector of the body, m $[kg]$ is mass of the tugboat, and $\vec{F}$ $[N]$ is external force vector acting on tugboat and t is the time in seconds, $\vec{\varpi}$ $[rad/s]$ the angular velocity vector, M $[kg.m^2]$ is the inertia matrix of the body and $\vec{H}$ $[N.m]$ is the external moment vector.

The contact force between the tugboat and the assisted ship is calculated with the contact coupling mechanism embedded in the DFBI module of STAR-CCM+. For the model to resemble a real contact, the contact force depends on the distance between the tugboat and the boundary (ship hull) at which the contact should be well idealized. The contact force is activated once this user-defined distance i.e., the effective range, is reached (Figure 2). As the tugboat gets near to the ship hull, the contact force increases until reaches a maximum value which stops the tugboat from moving further and avoid penetration. The contact force is applied on the mesh faces of the tugboat and the ship hull and may be calculated as

$$\vec{F}_f=F_n\hat{\imath}+F_t\hat{\jmath}\ , F_n=\vec{a}_f\left[k_1\left(d_0-d_f\right)-k_2\dot{d}_f\right]\ .\ \vec{n}_{bf}\ , \text{and } F_t=-\mu|F_n|\,tanh(\,k_tV_t) \tag{7}$$

where F_n $[N]$ and F_t $[N]$ is the normal and tangential component contact force, respectively; $\vec{a}_f$ $[m^2]$ is the face area vector, k_1 $[N/m]$ is the elastic coefficient, k_2 $[N.s/m]$ is the damping coefficient, d_0 $[m]$ is the effective range, d_f $[m]$ is the distance between the boundary face and the opposing boundary, $\vec{n}_{bf}$ is the normal vector to the boundary face, μ is the friction coefficient, k_t is the '*tanh*' coefficient, and V_t $[m/s]$ is the tangential velocity of the face f.

Two main defects in the STARCCM+ contact coupling mechanism should be overcome to resemble contact. At first, the contact force applied on the tugboat from the fluid cells is sensitive to the user-defined effective range. A considerably large effective range may lead to excessive rebounding of the tugboat after the first contact with the assisted ship. Thus, it should be adjusted at the start of the simulation, to avoid the magnification of the contact force. The other defect is that the software cannot model static friction when two bodies are in contact. Hence, regardless of the value of the tangential component of the contact force between the two bodies, they may slide over each other and wrongly idealize the loss of contact. To overcome the latter, a force is added at the center of gravity of the tug-

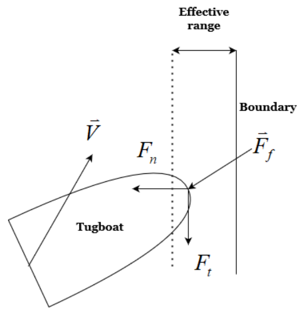

Figure 2. Contact coupling mechanism.

body which has the same magnitude, but opposite direction of the contact force, together with a counter moment to oppose the contact moment generated on the tugboat. These forces and moments are activated only when the contact force value is under the static friction value defined as

$$\vec{F}_{Ext} = \begin{cases} -\vec{F}_f & for\ F_t \leq \eta_{static} \cdot F_n \\ 0 & for\ F_t > \eta_{static} \cdot F_n \end{cases}, \text{ and } M_{Ext} = \begin{cases} -M_f & for\ F_t \leq \eta_{static} \cdot F_n \\ 0 & for\ F_t > \eta_{static} \cdot F_n \end{cases} \tag{8}$$

where $\vec{F}_{Ext}$ and M_{Ext} are the counter force and moment respectively, and η_{static} is the static friction coefficient between the tugboat fenders and the assisted ship side shell is assumed as steel.

2.3. Propeller idealization

To avoid high computational costs, the propeller was substituted by a virtual disk model. The virtual disk force is inserted as a source term in the momentum equations. As defined in STAR - CCM+ the source term comprises of a volume force $\vec{F}_b$ distributed over the cylindrical virtual disk, with an axial component f_{bx} and radial component $f_{b\theta}$ following the Goldstein optimum method [23] according to

$$f_{bx} = A_x r^* \sqrt{1 - r^*}, \text{ and } f_{b\theta} = A_\theta \cdot \frac{r^*\sqrt{1-r^*}}{r^*(1-r_h')+r_h'}; \text{ where } \{r^* = \frac{r'-r'}{1-r_h'}\ ;\ r_h' = \frac{R_H}{R_P} \text{ and } r' = \frac{r}{R_P}\} \tag{9}$$

where r is the radial coordinate, R_H is the hub radius, R_P is the propeller tip radius, and the radial distribution of the body forces is r^*. Both A_x and A_θ are constants computed from the propeller thrust T and torque Q as $A_x = \frac{105}{8} \cdot \frac{T}{\pi\Delta(3R_H+4R_P)(R_P-R_H)}$ and $A_\theta = \frac{105}{8} \cdot \frac{Q}{\pi\Delta R_P(3R_H+4R_P)(R_P-R_H)}$ where Δ represents the virtual disk thickness.

2.4. Tug Force Equilibrium Model (TFE)

The TFE is a model that assumes that the tug while pushing an assisted vessel reaches a steady equilibrium. Based on this idealization the contact force may be calculated as a summation of the hydrodynamic forces acting on the tugboat as follows

$$\begin{gathered} X_H + X_P + X_r = X_c \\ Y_H + Y_P + Y_r = Y_c \\ N_H + N_P + N_r = N_c \end{gathered} \tag{10}$$

where X, Y respectively represent the surge and sway forces, N is the yaw moment, subscripts H, P, R, and C represent the forces of the hull, propeller, rudder and contact, respectively. With the TFE model, the body is fixed and a steady CFD RANS simulation is conducted. Such idealization allows for reduced computational costs in comparison to the DFBI simulation that is transient.

Results presented in this paper correspond to the case of a conventional tugboat with single screw propeller and rudder configuration. The general particulars of the vessel are shown in Table 1. In 2D, the model scale $\lambda = 1/25$ and $Fn = 0.0602$ were used to reduce the computational effort. The data on the propeller geometry and characteristics were limited to the propeller hub/tip diameters and the number of blades. The propeller type chosen was a Wageningen B-series of an expanded area ratio $A_E/A_0 =$ 0.8 and pitch to diameter ratio $P/D = 1.1$. The performance curves used were based on [24] and are shown in Figure 3. The pushing operational scenario shown in Figure 4 assumes the case whereby two tugboats are pushing the assisted vessel with the same force. Accordingly, the assisted vessel has a constant heading. Both tugboats are moving with a constant velocity and a heading like the assisted vessel.

Table 1. Tugboat general particulars.

Dimension	Value	Unit
Length overall (LOA)	32.9	m
Length between perpendiculars (L_{PP})	30	m
Breadth molded	10	m
Depth molded	5.72	m
Maximum draft	4.75	m
Engine power	2880	KW
Bollard pull	39(382.5)	tons (KN)
Maximum speed	14 (7.2)	Knots (m/s)
Estimated operational speed during pushing	2(1.03)	Knots (m/s)

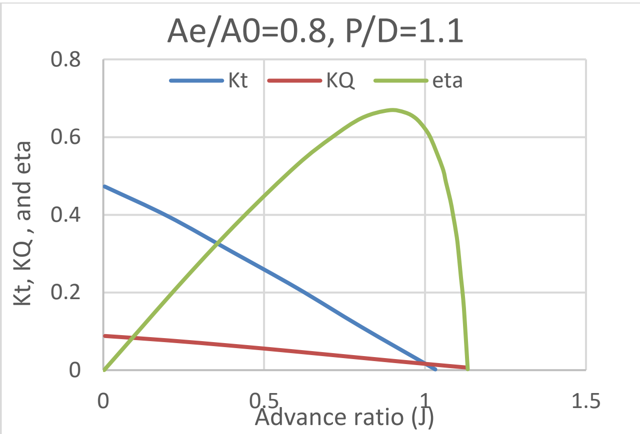

Figure 3. Propeller characteristics

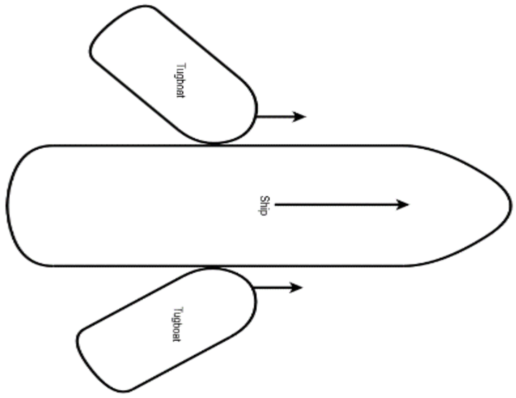

Figure 4. Pushing assistance scenario

Three cases of tugboat pushing operations were considered. In all cases, the influence of free surface hydrodynamics was disregarded as vessel and tug speeds were low. For the first two cases, results were based on a 2D model for which the assisted vessel was replaced by a rectangle and the propeller was idealized by a user-defined thrust force. The purpose of the exercise was to test the ability of the proposed DFBI model to predict the contact force as compared to a traditional equilibrium model. Figure 5 shows the domain dimensions for case 1 that utilizes the DFBI model in 2D. The tugboat overset region is set as a 2 degrees of freedom (DOF) body while the plate overset region representing the contact shell of the assisted ship is set as an 1 DOF body. The background region is assumed stationary. Case 2 applies the TFE model in which both the ship and the tugboat are assumed stationary. The fluid is flowing from the inlet and goes around the two bodies (Figure 6). Case 3 is based on a 3D idealization for which a TFE model is used to predict the contact forces on the tugboat at different velocities and drift angles (Figure 7). The tugboat has a zero heading while the inlet flow is set with an angle of attack equal to the drift angle required for a simulation. Such modelling approach helps simplify the meshing as compared to the case when the tugboat is rotated to a certain drift angle. Various boundary conditions were set along the lines for 2D models and on surfaces in 3D models. Tables 2, show the boundary conditions for each case. It is noted that $\vec{V}_{\infty}$ and θ_{spec} are user-defined values of the flow velocity and its direction, respectively. During modelling it was assumed that there is nothing predefined in way of the overset boundaries.

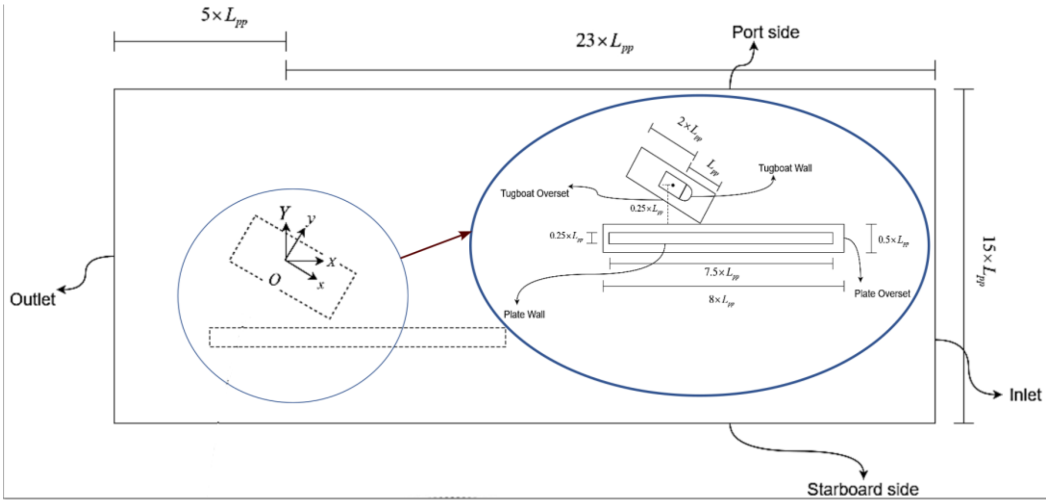

Figure 5. Case 1 domain dimensions

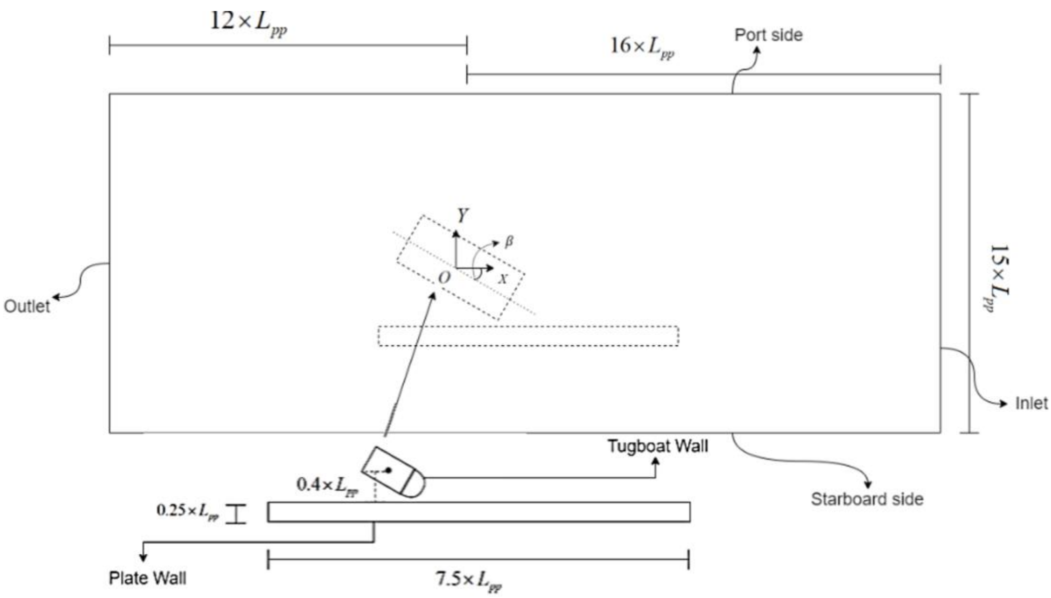

Figure 6. Case 2 domain dimensions

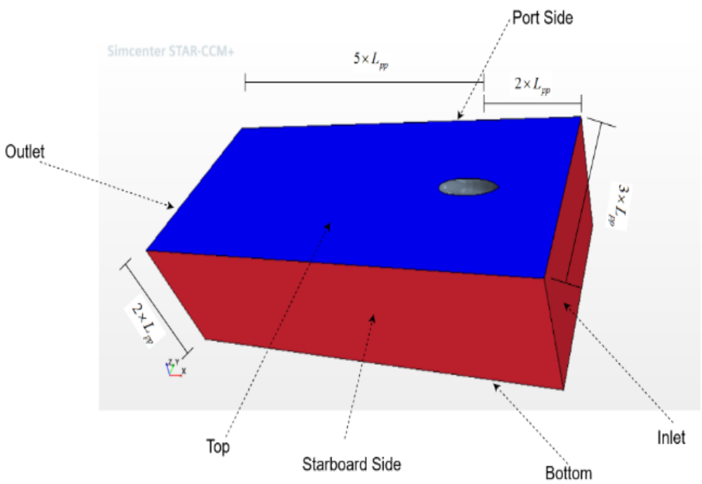

Figure 7. Case 3 domain dimensions

Table 2. : Boundary conditions

Region	Line/surface name	Velocity	Pressure	Motion specification
Case 1				
Background	Inlet	$V = 0$	Zero Gradient	Stationary
	Outlet	-	$P = 0$	
	Starboard Side	Symmetry	Symmetry	
	Port Side	Symmetry	Symmetry	
Tugboat	Tug Overset	-	-	DFBI translation (2DOF) (X, Y)
	Tugboat wall	$V = \vec{V}_{wall}$	-	
Plate	Plate Overset	-	-	Translation 1 DOF X
	Plate Wall	$V = \vec{V}_{wall}$	-	
Case 2				
Domain	Inlet	$V = \vec{V}_{\infty}$	Zero Gradient	Stationary
	Outlet	-	$P = 0$	
	Starboard Side	Symmetry	Symmetry	
	Port Side	Symmetry	Symmetry	
	Tugboat wall	$V = \vec{V}_{wall}$	Zero Gradient	
	Plate Wall	$V = \vec{V}_{wall}$	Zero Gradient	
Case 3				
Domain	Inlet	$V = \vec{V}_{\infty} \cdot \theta_{spec}$	Zero Gradient	Stationary
	Outlet	-	$P = 0$	
	Starboard Side	$V = \vec{V}_{\infty} \cdot \theta_{spec}$	Zero Gradient	
	Port Side	$V = \vec{V}_{\infty} \cdot \theta_{spec}$	Zero Gradient	
	Tugboat wall	$V = V_{wall}$	Zero Gradient	
	Bottom	$V = \vec{V}_{\infty} \cdot \theta_{spec}$	Zero Gradient	
	Top	Symmetry	Symmetry	

Polyhedral and hexahedral volume meshes were considered. The polyhedral mesh consists of arbitrary polyhedral-shaped cells. In this case, each individual cell has multiple neighbors. Hence, gradients may be accurately approximated. Polyhedral idealizations provide smooth transition between the prism layers and the rest of the volume mesh, albeit at the cost of larger number of cells as compared to hexahedral meshes [25]. A polyhedral mesh allows for the affordable use of many cells and may therefore be considered more appropriate for the 2D cases Figure 8. A hexahedral mesh is a template mesh comprising of cells that cut through the input geometry and may be more useful in 3D idealizations (Figures 9-10). Irrespective to the type of mesh used near to boundary walls layers of relatively small orthogonal prismatic cells should be formed. In this study the number of prismatic layers, their thickness and thickness distributions were controlled to achieve the desired range of $y+$ values as much as practically possible. The overlapping mesh technique was employed for the DFBI model. The moving bodies in such cases have an independent mesh domain that overlaps the main background domain. The outer region of the overlapping domain may exchange the flow characteristics with the background domain present at every step of the simulation.

For cases 1,2 there is a refined region along the length and width of $5 \times L_{pp}$ of the domain. The cell size in the refined region was set to be near or equal to the size of the overlapping mesh. In case 3, two sub-regions were refined namely (a) a region along the length of the domain with width of $5 \times L_{pp}$ and a depth of $Max.draft + 1m$ (same as in 2D cases) and (b) a cylindrical domain before and beyond the location of the virtual disk. The latter idealization accounts for abrupt flow changes.

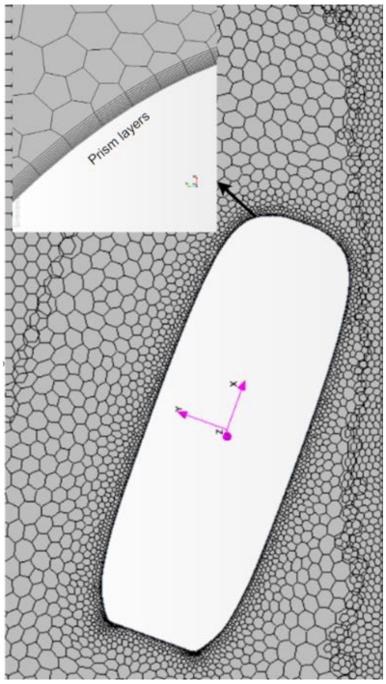

Figure 8. The prismatic layers around the hull for case 1 and case 2.

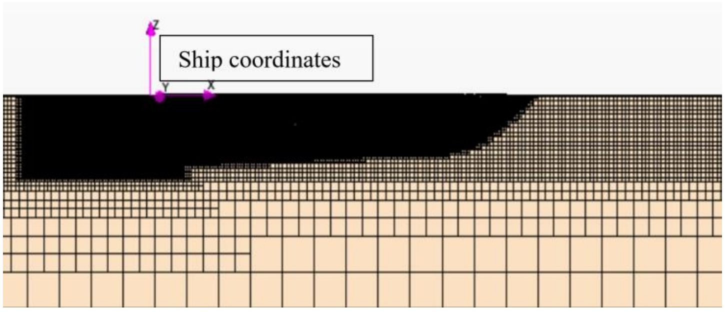

Figure 9. Case 3 refined regions along the depth

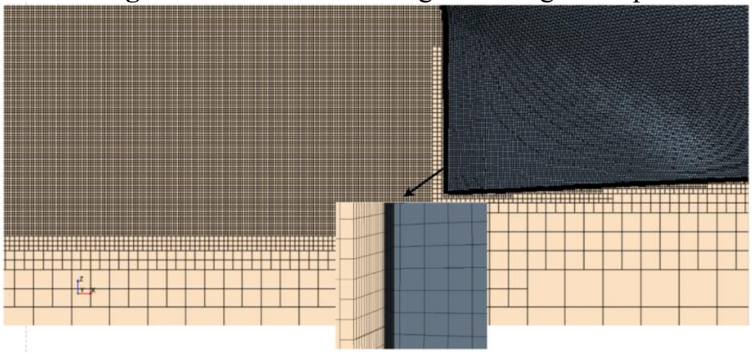

Figure 10. Case 3 virtual disk refined region and prism layers

3. Verification of computational models

In cases 1,2 the behavior of the DFBI and the TFE models was assessed and compared with the aim to confirm that the TFE model idealizes accurately the contact forces. Hence, the results are discussed only qualitatively and have not been compared to the 3D results. For case 3, the results are discussed qualitatively and quantitatively. The main sources of error and hence uncertainty consisted of the iteration error of the discretized equations, the grid resolution and the time step error for unsteady simulations, and other residual sources of error. The study focused on verifying the model in terms of the truncation error, i.e., the model is verified by assessing the mesh uncertainty of the simulations. The tool applied made use of the Richardson extrapolation method [26]. A convergence study using multiple solutions of different mesh resolutions with a uniform refinement ratio of $\sqrt{2}$ was carried out. Drift angle and velocity were kept constant at 15 degrees and 2 knots, respectively. The solution parameter on which the convergence study was performed has been the drag value. Three meshes were used with number of cells and drag solutions as shown in Table 3.

Table 3. Mesh uncertainty data

Refinement ratio	Base Size (m)	Number of cells	Drag	Unit	Solution symbol
	4.5	14.1 million	2395	N	S_1
$\sqrt{2}$	6.363	7.7 million	2450	N	S_2
	9	4.1 million	2930	N	S_3

The error estimate between the solution at the finest grid and the estimated exact solution S_0 at the infinitesimal base-size was defined as

$$\delta_{RE} = S_1 - S_0 = \frac{S_2 - S_1}{r^p - 1} = 7.1\ N \tag{11}$$

where r is the refinement ratio, and $p = 6.25$ is the order of the curve. The error estimate was eventually multiplied by a factor of safety of 1.25 to limit the simulation error to be $U_G = C\delta_{RE} = 1.25\delta_{RE} =$

8.89N. Although the error at the finest mesh is minimal, a medium mesh resolution (base size=6.36) was used for the simulations to reduce the computation time.

4. Results and discussion

This section presents the results of the hull hydrodynamic, thrust and contact forces acting on the tugboat for each studied case. Then, results of case 3 are used to form decision-making charts to be used by tug masters. For cases 1,2, the simulation time was 100 seconds with a time step of 0.05 seconds. The simulation scenario assumed that the tugboat is initially positioned at some distance from the ship. During the first impact, the contact force dramatically increased. Eventually, the tugboat moved out of the effective range due to rebounding, so the contact force diminished. The bounding and rebounding actions lasted for 20 seconds until the tugboat reached a steady contact with the plate and almost constant contact force values. After another 20 seconds, the contact forces started to change and fluctuate about a mean value. The force summation (Figure 11) shows that despite the variation of the contact and hydrodynamic forces the thrust force remained constant at zero. This means that any increase in the hydrodynamic force can be followed by a contact force decrement in the same direction. This observation supports the use of the TFE model in predicting contact forces. It also suggests that the variation of the contact force can be linked directly to the change in fluid actions on the tugboat.

The contact force variation in both cases follows the same trend. This reflects the strong dependency on hull forces. The mean forces show a difference of less than 2.5% (Figures 12, 13). The Y components of contact forces from case 1 lag those of case 2 (Figure 13). This reflects ship dynamics during the unsteady bounding / rebounding initial phase of contact that lasted for 20 seconds. For case 3, a set of 16 steady simulations over 2-5 knots and drift angles from 15 to 60 degrees were considered. Case 3 results are shown in Figure 14–18. A plot of the drag force against the drift angle for a range of velocities is depicted in Figure14. The drag increased with increasing velocity. The differences in the drag forces for the speed range considered at low drift angles was not significant. As the drift angle increased, this difference was dramatically raised. The speed increased proportionally to drag.

Figure 15 displays the variation of the sway force with the drift angle at different velocities. The sway force generally increased until the drift angle reached 45 degrees. After this point it decreased as the speed increased. When the sway force acted in the negative direction, the pushing force increased. Although the increase in the speed might cause a rise in the drag force and reduce pushing, it led to an increase of sway forces in the negative direction. This means that from an operational perspective the speed and drift angles should be kept at optimum levels to reach an ideal pushing force. The thrust coefficient variation against the drift angle is shown in Figure 16. As expected, it declined by increasing the speed, whereas it was slightly varied at the same speed with changing the drift angle. To get the maximum thrust available for pushing, the speed must be kept to a minimum. Figures 17 and 18 demonstrate the variation of the components of the pushing forces.

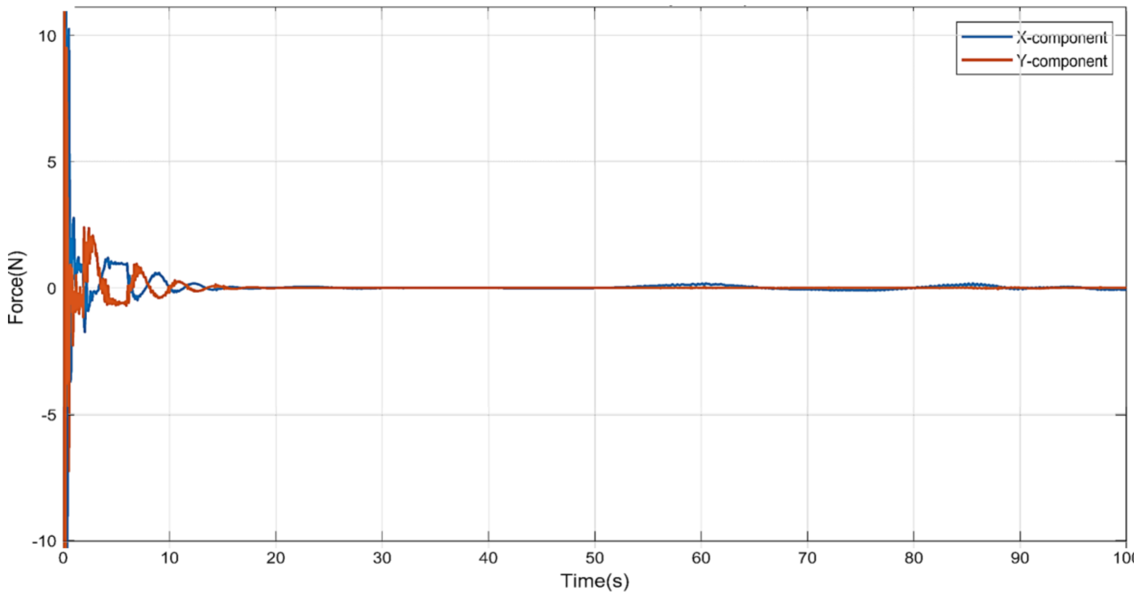

Figure 11. Force summation in the X, and Y directions.

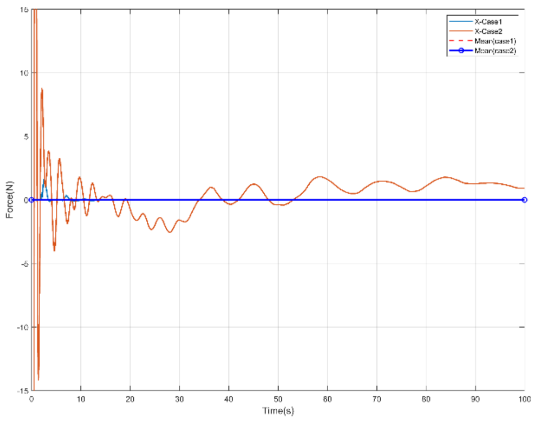

Figure 12. X component of the contact force in case 1 and case 2.

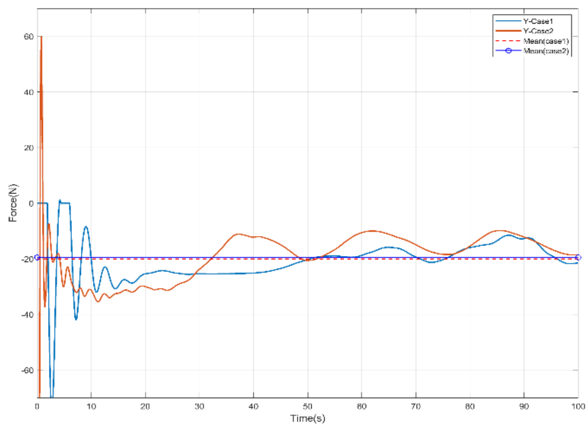

Figure 13. Y components of the contact force in case 1 and case 2.

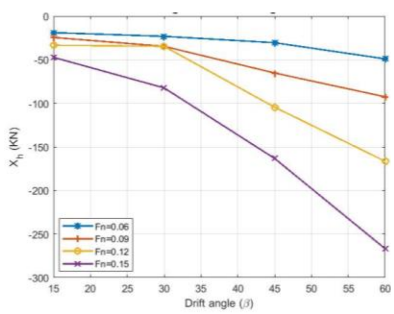

Figure 14. Drag versus drift angle

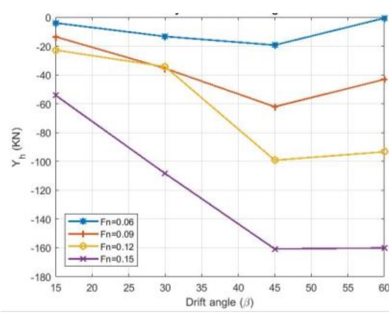

Figure 15. Sway force versus drift angle

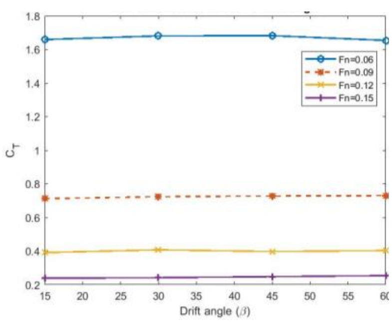

Figure 16. Thrust coefficient vs drift angle

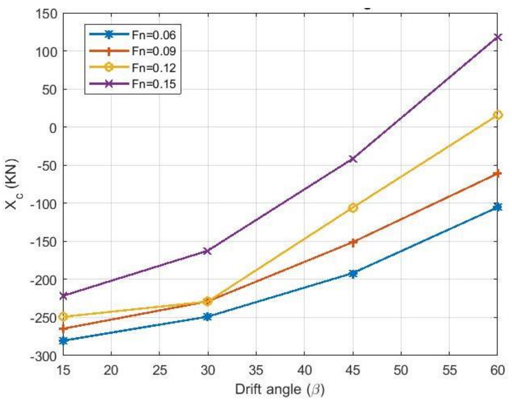

Figure 17. X component of the contact force

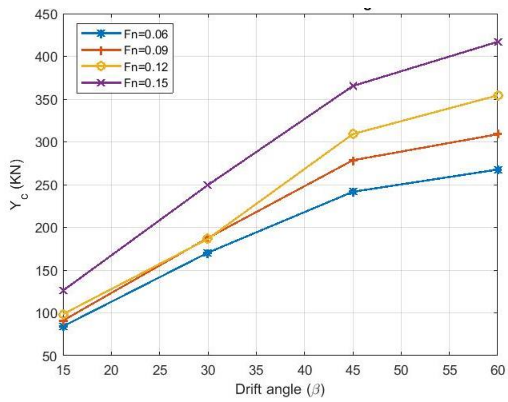

Figure 18. Y component of the contact force

4.1. Stability Against Sliding

Stability against sliding was determined by studying (i) whether the contact force on the tugboat is enough for sliding to occur and (ii) observing the variation of the critical angle at each velocity before sliding. The sliding condition states that the x-component of the contact force must be lower than the y-component multiplied by the static friction coefficient to avoid sliding $X_c \leq \eta \cdot Y_c$. Figures 19-22 demonstrate the range of stability against sliding using three friction coefficient values. The lower the angle at the intersection of the sliding curve with the x-axis, the higher the stability range without sliding. At low drift angles, the tugboat was unstable for the whole range of velocities. However, as the drift angle increased, the Y-component contact force increased, and the X-component contact force decreased until the critical angle of 45 degrees. Generally, speed increase widened the stability range against sliding. This could be attributed to the fact that the critical angle decreased.

4.2. Tug Performance Charts

The pushing forces and sliding curves were used to generate the tug performance charts (see Figure 23-26). The pushing force is presented in the polar coordinates (r,θ) instead of the cartesian coordinates to facilitate the decision making. At any point on the pushing force line, the r-component represents the pushing force value in tons, while the θ-coordinate represents the drift angle. The straight lines shown indicate whether the condition is stable against sliding or not. There are three different straight lines for each of the friction coefficient values. The region on the right side of the straight line represents the unstable area in which sliding will occur, and the tug master is recommended to use the rudder to return the tugboat to its required position. The left side of the friction coefficient line is expected to be stable; there is no need for the tug master to involve. The intersection point between friction coefficient lines and the pushing force line represents the critical angle.

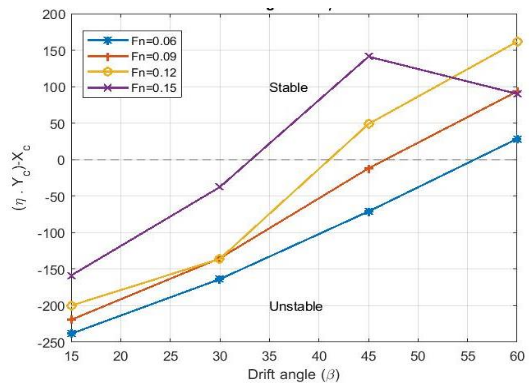

Figure 19. Sliding curves at static friction coefficient = 0.5

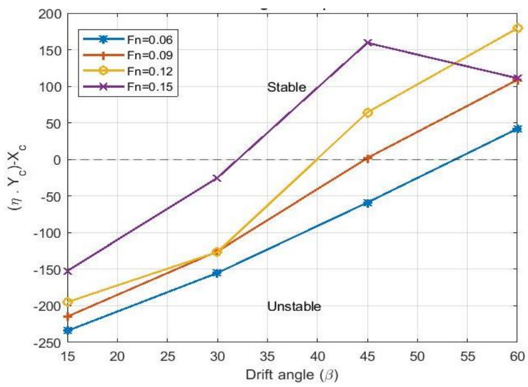

Figure 20. Sliding curves at static friction coefficient = 0.55

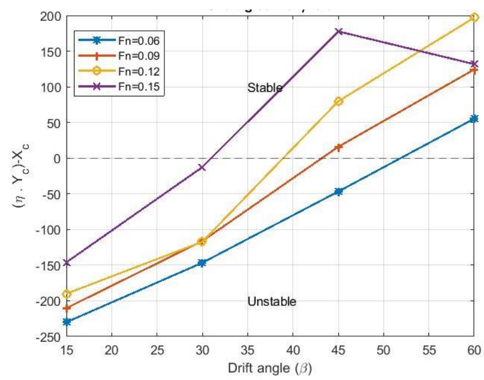

Figure 21. Sliding curves at static friction = 0.6.

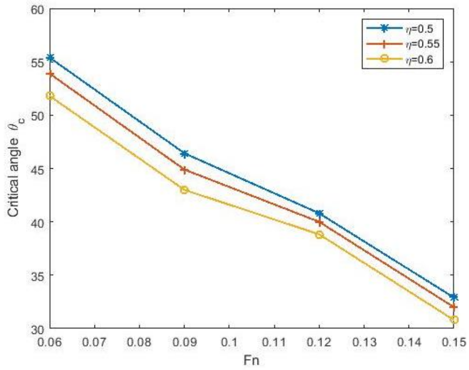

Figure 22. Critical angle against velocity.

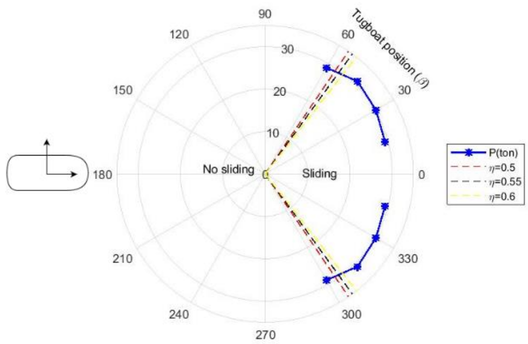

Figure 23. Pushing performance chart at 2 knots

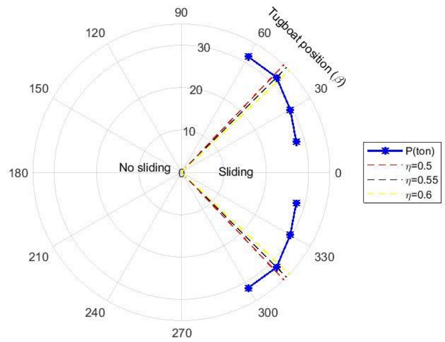

Figure 24. Pushing performance at 3 knots.

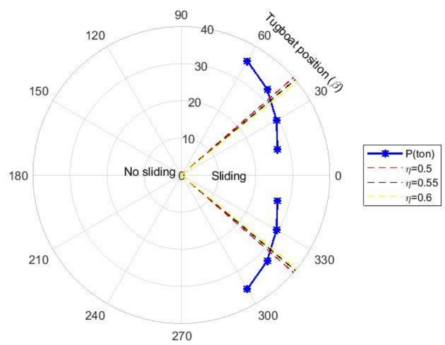

Figure 25. Pushing performance at 4 knots.

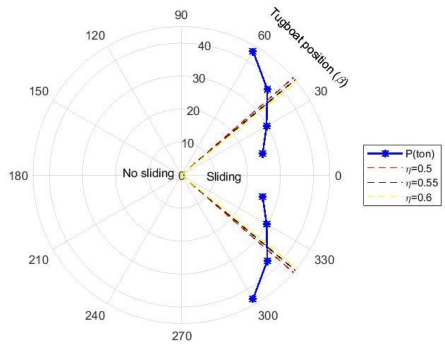

Figure 26. Pushing performance at 5 knots

5. Conclusions

This paper presented an investigation on the pushing performance of tugboats during ship assistance operations using CFD. The contact forces that act on the tugboat were predicted using two models. The first model applied an unsteady RANS CFD method with DFBI module and the contact mechanics coupling module in the STARCCM+ solver to simulate the contact between the two vessels and the tug motions. The second model utilized the same solver with either a steady or unsteady RANS method but without the DFBI and the contact mechanics coupling modules. A comparison of the contact forces predicted between the two models showed that the DFBI might be more elaborative in capturing the time variations of the contact forces. However, the tug force equilibrium model is more economic.

A set of 16 steady RANS simulations was conducted with the aim to predict the mean values of the contacts force acting on the tugboat and to develop decision-making charts. The simulations were conducted for a range of drift angles from 15 to 60 degrees and a speed range from 2 to 5 knots. Overall, the results demonstrated that the proper choice of orientation and speed of the tugboat might increase the pushing force to levels of its bollard pull and even more as the hull forces in such cases are supplementing the propeller forces. Comparison of results suggests that the DFBI model is able to capture well the contact coupling mechanism and could be employed for the derivation of more detailed decision-making charts for use in ship handling operations.

6. Acknowledgements

The authors wish to acknowledge CSC – IT Center for Science, Finland, for the provision of parallel computing computational resources used in this study and Alfons Hakans tug operators for the useful discussions during the preparation of this manuscript.

References

[1] Viran A and Mentes A 2021 Assessment of propulsion systems performance in tugboat *GİDB Dergi (Istanbul Tech. Univ.)* 53 – 66
[2] Taguchi H, Haraguchi T, Minami M and Houtani H 2015 An investigation into the capsizing accident of a pusher tug boat *12th International Conference on the Stability of Ships and Ocean Vehicles STAB 2015* (Glasgow) pp 903–910
[3] Lahtinen J, Valdez Banda O A, Kujala P and Hirdaris S 2020 Remote piloting in an intelligent fairway – A paradigm for future pilotage *Saf. Sci.* **130**
[4] HELCOM – Baltic Marine Environment Protection Commission 2011 *Report on shipping accidents in the Baltic Sea area during 2011.* (Helsinki, Finland)
[5] HELCOM – Baltic Marine Environment Protection Commission 2018 *Report on shipping accidents in the Baltic Sea from 2014 to 2017.* (Helsinki, Finland)
[6] Butt N, Johnson D, Pryce-roberts N and Vigar N 2015 15 Years of Shipping Accidents : A review for WWF Southampton Solent University *Shipp. Accid. Rep.* **44** 37–63
[7] Vantorre M, Eloot K, Delefortrie G, Lataire E, Candries M and Verwilligen J 2017 Maneuvering in shallow and confined Water *Encyclopedia of Maritime and Offshore Engineering* (John Wiley & Sons, Ltd) pp 1–17
[8] Piaggio B, Villa D and Viviani M 2020 Numerical analysis of escort tug manoeuvrability characteristics *Appl. Ocean Res.* **97** 102075
[9] Figari M, Martinelli L, Piaggio B, Enoizi L, Viviani M and Villa D 2020 An All-Round Design-to-Simulation Approach of a New Z-Drive Escort Tug Class *J. Offshore Mech. Arct. Eng.* **142**
[10] Piaggio B, Viviani M, Martelli M and Figari M 2019 Z-Drive Escort Tug manoeuvrability model and simulation *Ocean Eng.* **191** 106461
[11] Simonsen C D, Nielsen C K, Otzen J F and Agdrup K 2011 CFD based prediction of ship-ship interaction forces on a TUG beside a tanker *RINA, Royal Institution of Naval Architects - 2nd International Conference on Ship Manoeuvering in Shallow and Confined Water: Ship to Ship Interactions 2011* pp 329–38
[12] Sutulo S and Guedes Soares C 2009 Simulation of close-proximity maneuvers using an online 3D potential flow method *MARSIM '09 Conference, Proceedings* pp M-9-1/10
[13] Lataire E, Vantorre M and Delefortrie G 2009 Captive model testing for ship to ship operations *MARSIM 09 Conference Proceedings* pp M-14-1/10
[14] Falter J 2010 *Validation of a potential flow code for computation of ship-ship interaction forces with captive model test results*
[15] Jayarathne N, Ranmuthugala D, Leong Z, Fei J, Chai S and Chen H M 2019 Numerical and experimental prediction of hydrodynamic interaction effects acting on tugs during ship manoeuvres *J. Mar. Sci. Technol.* **27** 185–201

[16] Jayarathne B, Ranmuthugala D, Chai S and Fei J 2014 Estimation of Drag Force on Tug Hulls at Different Drift Angles *3rd International Symposium of Maritime Sciences* pp 10–4
[17] Stickings T, Griffith K, Mitchell C, Wright J and Patel B 2021 MailOnline *dailymail*
[18] Håkans A 2020 Icebreaking
[19] Xu D, Zhang X and Yin Y 2016 The computer simulation study of tug pushing operation system *Chinese Control Conference, CCC* vol 2016-Augus (Chengdu, China: IEEE) pp 2074–80
[20] Artyszuk J 2013 Simplified steady-state analytical model for manoeuvring and control of ASD tug in escort push operations *Zesz. Nauk. / Akad. Morska w Szczecinie* **nr 36 (108** 5–14
[21] Menter F R 1994 Two-equation eddy-viscosity turbulence models for engineering applications *AIAA J.* **32** 1598–605
[22] Kundu P K and Cohen I M 2002 *Fluid Mechanics* (California: Elsevier)
[23] S. Goldstein 1929 *On the vortex theory of screw propellers* (London)
[24] Bernitsas M M, Ray D and Kinley P 1981 *KT, KQ and efficiency curves for the Wageningen B-series propellers*
[25] Sosnowski M, Krzywanski J, Grabowska K and Gnatowska R 2018 Polyhedral meshing in numerical analysis of conjugate heat transfer *EPJ Web Conf.* **180**
[26] Resistance Committee of 23rd International Towing Tank Conference 2002 *ITTC - Recommended Procedures and Guidelines Uncertainty Analysis in CFD ,Verification and Validation Methodology and Procedures*